J Mater Sci: Mater Electron (2024) 35:1220

Enhanced photocatalytic activity in AgCu-decorated ZnO nanoparticles under UV and sunlight

Abd Elouahab Noua[1,*], Dogan Kaya[1,2], Gokmen Sigircik[3], Tunc Tuken[3], Faruk Karadag[1], and Ahmet Ekicibil[1]

[1] *Department of Physics, Faculty of Art and Sciences, Cukurova University, Adana, Turkey*
[2] *Department of Advance Materials and Nanotechnology, Graduate School of Sciences, Cukurova University, Adana, Turkey*
[3] *Department of Chemistry, Faculty of Art and Sciences, Cukurova University, Adana, Turkey*

Received: 12 December 2023
Accepted: 6 June 2024

© The Author(s), 2024

ABSTRACT

This study investigates the structural, morphological, and photocatalytic properties of monometallic (Ag and Cu) and bimetallic (AgCu) nanoparticles (NPs) incorporated into ZnO NPs and their photocatalytic performance. X-ray diffraction and Rietveld refinement were employed to analyze the structural characteristics, revealing the formation of a hexagonal wurtzite structure of ZnO and cubic phases of Ag and Cu within the metal-decorated NPs. Scanning electron microscopy provided visual evidence of the spherical morphology, with an average particle size of 50 nm. Energy-dispersive X-ray spectroscopy confirmed the successful deposition of Ag, Cu, and AgCu NPs onto the ZnO surface. The photocatalytic efficiency of the NPs was evaluated by the degradation of methylene blue dye under UV light at a wavelength of 254 nm under sunlight irradiation. Under UV light, the bimetallic AgCu/ZnO system exhibited exceptional performance, achieving a degradation rate of about 95% with 10% AgCu/ZnO. Conversely, under sunlight illumination, the monometallic Cu/ZnO and Ag/ZnO NPs exhibited outstanding photocatalytic properties, with degradation rates of about 99 and 98%, respectively. These findings underscore the influence of the light source on photocatalytic performance as well as the significance of the plasmonic effects and charge-transfer mechanisms.

1 Introduction

Surface water pollution from industrial discharge caused by hazardous compounds, including dyes, pesticides, pharmaceutical ingredients, fertilizers, etc., and organic dyes poses a critical threat to human health and the environment due to their importance in the industrial field with a wide range of applications [1, 2]. To address this issue, photocatalysis has emerged as a highly effective and environmentally friendly method for the decomposition of organic dyes into CO_2 and H_2O. Various materials have been used for the photocatalytic degradation of the organic dyes since the discovery of TiO_2 photocatalytic water splitting by Fujishima and Honda in 1972, including metal oxides, metal chalcogenides, and carbon nanotubes have been

Address correspondence to E-mail: noua.abdelouahab@gmail.com

https://doi.org/10.1007/s10854-024-12919-4
Published online: 23 June 2024

used for photocatalytic degradation of organic dyes [3–6]. ZnO has emerged as a prominent topic of interest among these materials owing to its remarkable photocatalytic efficiency, biocompatibility, and cost-effectiveness [7]. Consequently, substantial efforts have been directed toward enhancing photocatalytic performance [8, 9].

Despite its advantages, ZnO exhibits limitations, such as a wide band gap resulting in limited activity in the visible region, a low concentration of photogenerated electron–hole pairs (e/h), and rapid recombination of these charge carriers. Various strategies have been proposed to overcome these challenges, including elemental doping with metals and non-metals [10–14] to augment the charge carrier densities and modify the optical properties. Additionally, coupling ZnO with other materials to form heterostructures has been explored to improve visible-light absorption and facilitate charge separation, thereby mitigating fast recombination [15, 16]. Furthermore, loading or decorating ZnO with noble metals has been demonstrated to enhance visible-light absorption and promote charge separation [17, 18]. Notably, at the nanoscale, the particle size, shape, and morphology significantly influence the specific surface area, light absorption wavelengths, and overall photocatalytic performance [19, 20].

Therefore, careful selection of the preparation method and precise control of the synthesis conditions are crucial. Various techniques have been employed to synthesize ZnO nanoparticles, including the sol-gel [21], thermal decomposition [22], hydrothermal [23], and polyol process [24]. Among these methods, the polyol process stands out for its cost-effectiveness, simplicity, ability to control particle size, shape, and morphology, and capability to load and decorate mono and bimetallic nanoparticles onto support materials without oxidation.

Loading mono and bimetallic nanoparticles onto ZnO has proven effective in enhancing visible light absorption, particularly in the case of plasmonic metals such as Ag and Au. This approach improves catalyst stability and reduces charge recombination through interfacial charge carrier transfer [25–27]. Plasmon-induced catalytic reactions can take place directly, where plasmonic nanostructures act as both light absorbers and catalytically active sites, or indirectly, by harvesting light while in contact with a photocatalyst. Several strategies have been employed to maximize the utilization of sunlight energy, including the selection of appropriate plasmonic materials, manipulation of nanostructure morphology, and control of the particle size [28].

Moreover, non-noble metals have shown promise for enhancing photocatalytic activity. For instance, 3 and 5% Cu-doped ZnO demonstrated superior photocatalytic activity [29]. Cu-loaded ZnO nanorods exhibited nearly six-fold higher photocatalytic efficiency than bare ZnO nanorods [30]. Bimetallic $Cu_{75}Ni_{25}$-decorated zinc oxide demonstrated fivefold faster methylene blue degradation under sunlight than mono noble metals such as Pt, Au, and Ag, with an extended electron–hole lifetime of 38.12 ns [31]. This study elucidates the role of plasmonic effects and charge-transfer mechanisms in enhancing the photocatalytic activity by the synthesis of mono Ag, Cu, and bimetallic AgCu with different concentration 5 and 10% nanoparticles loaded onto ZnO NPs using a modified polyol method. The synthesized nanoparticles were comprehensively characterized using various techniques to investigate their structural, morphological, and optical properties. Finally, their photocatalytic activity was evaluated under both UV and natural sunlight irradiation using methylene blue dye as a model for organic pollutant degradation.

2 Experimental

2.1 Chemicals

Zinc acetate dihydrate ($Zn(CH_3COO)_2{\cdot}2H_2O$), silver nitrate ($AgNO_3$), and copper(II) acetylacetonate ($Cu(C_5H_7O_2)_2$) were used as precursors, with ethylene glycol (EG) and sodium borohydride ($NaBH_4$) as the initial and high temperature reducing agents, respectively. Sodium hydroxide (NaOH) was added to adjust the pH to approximately 9.5–10. Polyvinylpyrrolidone (PVP, M 40000) was used as the capping agent to prevent oxidation and agglomeration. Prior to introducing the precursors into EG, they were dissolved in N, N-Dimethylformamide (DMF) to create a homogeneous mixture. The final product was washed with ethanol. All chemicals used in this study were purchased from Sigma-Aldrich and were utilized as received without further purification.

2.2 Synthesis of ZnO NPs

To prepare 0.1 M ZnO, zinc acetate dihydrate ($Zn(CH_3COO)_2{\cdot}2H_2O$) was dissolved in 20 mL of EG in a three-neck flask, 0.2 M PVP was added to prevent the agglomeration of NPs. Deionized water with a fixed hydration ratio h = H_2O/Zn = 6 was added to the mixture. The solution was magnetically stirred under an Ar gas atmosphere and gradually heated to 185 °C, and maintain at this temperature for 30 min before cooling the solution to room temperature. To collect the nanoparticles, the final product was washed with ethanol and deionized water, followed by centrifugation at 9000 rpm for 6 min per cycle. Subsequently, the obtained nanoparticles were calcinated at 500 °C for 1 h.

2.3 Synthesis of Ag, Cu, and AgCu NPs on ZnO

The Ag, Cu, and AgCu NPs were synthesized on ZnO using modified polyol process [32]. In a typical synthesis, $[Ag^+]/[Zn^{2+}]$ was maintained at 0.05 mol% to achieve 5% Ag loading on ZnO. Initially, an appropriate amount of the Ag precursor ($AgNO_3$) was dissolved in 5 mL of DMF and then added to a solution of EG containing 0.1 g of the prepared ZnO. NaOH (at a mole ratio of 15) and PVP (at a mole ratio of 2) were introduced into the solution, followed by refluxing the mixture at room temperature for 30 min. The resulting mixture was vigorously stirred under an argon gas atmosphere and heated to 120 °C. Subsequently, $NaBH_4$ dissolved in 5 mL DMF (at a mole ratio of 24) was added dropwise to the mixture. After reaching 160 °C, the reaction solution was maintained at this temperature for 30 min and then cooled to room temperature. The final product was washed with ethanol, centrifuged at 9000 rpm for 6 min per cycle, and dried at 80 °C. The obtained NPs were named as Ag/ZnO. The same procedure was employed to prepare 5% Cu/ZnO and 5% AgCu/ZnO and 10% AgCu/ZnO, denoted as Cu/ZnO, 5AgCu/ZnO and 10AgCu/ZnO, respectively.

2.4 Photocatalytic activity evaluation

The photocatalytic activity of the NPs was assessed by monitoring the decomposition of methylene blue (MB) dye in a pH 7 aqueous solution at room temperature using a lamp with a wavelength of 254 nm and power of 9W as a UV light source. In a typical photocatalytic experiment, 10 mg of the photocatalyst was dispersed in 50 mL aqueous solution containing 10 mg/L MB. The mixture was then stirred in the dark for 30 min to establish adsorption–desorption equilibrium between the photocatalysts and MB dye. Measurements were conducted by withdrawing 4 mL of the solution at 20-min intervals. Subsequently, the solution was centrifuged at 7000 rpm for 3 min to remove the photocatalysts, and the maximum absorption at 664 nm, corresponding to MB, was recorded using a Visible Spectrophotometer. Photodegradation efficiency (D) and rate constant (k) were calculated using the following equations [33, 34]:

$$D\,(\%) = \left(C_0 - C\right)/C_0 \times 100 \tag{1}$$

$$-\ln\left(C/C_0\right) = Kt \tag{2}$$

where (C_0) represents the initial concentration, (C) signifies the concentration at time (t), (K) denotes the pseudo-first-order kinetic constant, and (D) stands for the degradation rate.

3 Results and discussion

3.1 Structural properties

The structural analysis of pure ZnO, Cu/ZnO, Ag/ZnO, 5AgCu/ZnO and 10AgCu/ZnO NPs was initially performed using XRD diffraction patterns and Rietveld refinement analysis (see Fig. 1a, c and Supplementary Information Fig. S1). The XRD pattern of pure ZnO and 5AgCu/ZnO NPs are presented in Fig. 1a, c, which confirms the formation of ZnO hexagonal wurtzite crystal structure and Ag and Cu formation via Rietveld refinement analysis showing calculated patterns (red line), difference (blue line), and Bragg positions (black bars). The typical wurtzite structure exhibited 2θ values of 31.7°, 34.4°, 36.2°, 47.5°, 56.6°, 62.8°, 66.4°, 67.8°, 69.1° 72.5° and 76.9° corresponding to the lattice planes (100), (002), (101), (102), (110), (103), (200), (112), (201), (004) and (202), respectively. The presence of intense and sharp peaks indicates the excellent crystallinity of the prepared ZnO with high purity, confirmed by the absence of any impurity peaks, which is consistent with previous studies [35, 36]. In Fig. 1b, XRD diffraction peaks of pure ZnO (black), Cu/ZnO (red), Ag/ZnO (green), bimetallic

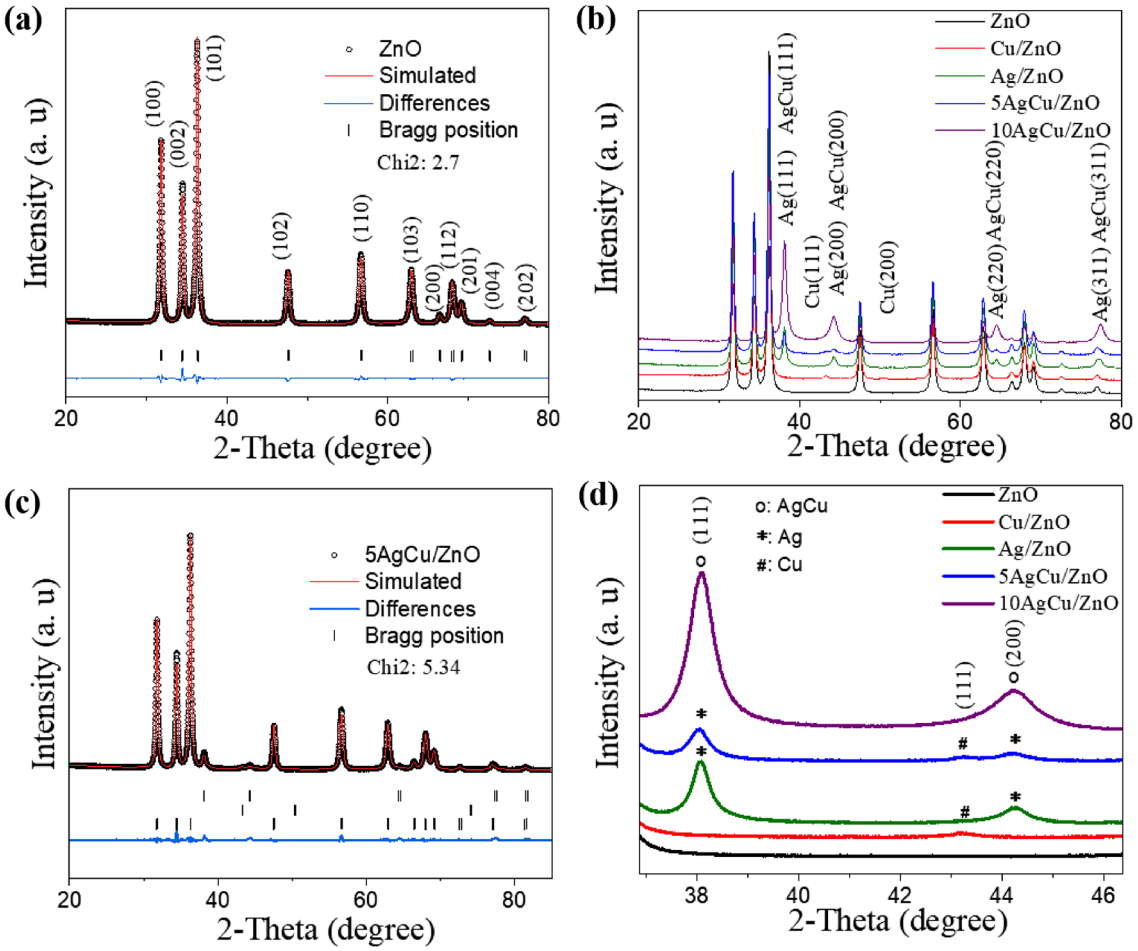


Fig. 1 The XRD diffraction patterns **a** pure ZnO and **c** 5AgCu/ZnO NPs (hollow circle) with Rietveld refinement analysis showing the calculated patterns (red line), difference (blue line), and Bragg positions (black bars). **b** XRD diffraction peaks of pure ZnO (black), Cu/ZnO (red), Ag/ZnO (green), and bimetallic AgCu/ZnO (blue) NPs. **d** Zoomed view showing Ag (*), Cu (#) and bimetallic AgCu (o) NPs peaks (Color figure online)

5AgCu/ZnO (blue) and 10AgCu/ZnO (blue) NPs are presented. These diffraction patterns reveal single Ag and Cu peaks alongside bimetallic AgCu phases in the structure. For monometallic Ag/ZnO NPs, the Ag peak positions were identified at $2\theta = 38.1°$, 44.3°, 64.5°, and 77.5°, corresponding to the (111), (200), (220), and (311) planes, respectively. In contrast, the monometallic Cu/ZnO NPs displayed only two peaks at 43.2° and 50.3°, corresponding to the (111) and (200) planes, respectively. The bimetallic 5% AgCu/ZnO exhibited both Ag (*) and Cu (#) formation on the ZnO surface (see Fig. 1d) [37–39]. However, 10% AgCu/ZnO NPs exhibited dominant AgCu (o) alloy phases at $2\theta = 38.1°$, 44.2°, and 64.5° which belong to (111), (200) and (220) planes (see Fig. 1d). The intensity of the Ag peaks decreased for 5AgCu NPs, indicating the incorporation of Cu into the Ag lattice signifying a certain degree of alloying, despite the presence of two separate phases [40]. Notably, the absence of any peaks corresponding to Ag_2O, CuO and Cu_2O phases confirms the formation of oxide-free AgCu bimetallic NPs. Furthermore, as shown in Fig. 1b the decrease in the intensity of the ZnO peaks confirms the coating of Ag, Cu and AgCu NPs on the ZnO surface.

The grain size was also estimated from the three most intense peaks for ZnO and from the (111) peak for Ag and Cu using the Debye–Scherrer equation and the different structural parameters of the NPs, including the crystallite size, *d*-space, and lattice parameters, were obtained from Rietveld refinement analysis and are summarized in Table 1. Notably, the structural parameters of ZnO did not change

Table 1 The structural parameters of the NPs were crystallite size (nm), d-space (Å), lattice parameter (Å), and particle size (nm)

Sample	Phase	Crystallite size (nm)	$d_{(111)}$-space (Å) (111) Ag/Cu (101) ZnO	Lattice parameter (Å)	Particle size (nm)
ZnO		26	2.47	3.24/5.20	50
Ag/ZnO	Ag	54	2.35	4.082	46
	ZnO	26	2.47	3.24/5.20	–
Cu/ZnO	Cu	46	2.09	3.625	59
	ZnO	27	2.47	3.24/5.20	–
5AgCu/ZnO	Ag	18	2.36	4.090	43
	Cu	56	2.09	3.620	–
	ZnO	26	2.47	3.25/5.20	–
10AgCu/ZnO	AgCu	15	2.36	4.088	49
	ZnO	26	2.47	3.25/5.21	–

significantly, confirming that mono-(Ag, Cu) and bimetallic AgCu were loaded only on the ZnO surface. ZnO's d(111)-space remained at 2.47 Å for all samples, consistent with the crystallite size D, which was approximately 26 nm. The higher intensity of the bimetallic AgCu compared to the Ag and Cu addition on the ZnO surface (see Fig. 1d) indicates their better crystallinity. The difference in the crystallite sizes of Ag and Cu can be attributed to the distinct nucleation rates during synthesis [41].

3.2 FTIR analysis

Figure 2 displays the FTIR spectra of pure ZnO (black), Cu/ZnO (red), Ag/ZnO (green) and bimetallic 5AgCu/ZnO (blue) NPs in the range of 4000–400 cm^{-1}. Several distinct absorption peaks were observed in the spectra. First, a broad peak at 3411 cm^{-1} is attributed to the symmetric stretching bonds of N–H, whereas the peak at 2900 cm^{-1} corresponds to the asymmetric stretching vibration of C-H. In the case of the as-prepared mono Cu, Ag, and AgCu bimetallic NPs, two distinct peaks were observed at 2327 cm^{-1} and 2115 cm^{-1}, along with a shoulder peak at 2666 cm^{-1} due to the presence of PVP [32]. The peak at approximately 1600 cm^{-1} can be attributed to the stretching of C=O bonds. Additionally, the peaks at 1048 cm^{-1} and 1390 cm^{-1} represent the absorption bands of C–H [25]. Peaks below 500 cm^{-1} are indicative the presence of ZnO within the structure, and corresponds to the Zn–O stretching vibrations.

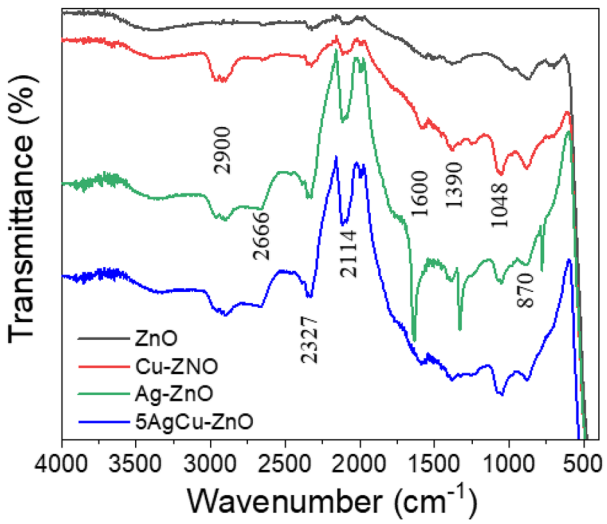


Fig. 2 FTIR spectra of pure ZnO (black), Cu/ZnO (red), Ag/ZnO (green) and bimetallic 5AgCu/ZnO (blue) NPs in the range of 4000–400 cm^{-1} (Color figure online)

3.3 Morphology properties

The morphologies of the pure ZnO, Ag, Cu and AgCu-decorated ZnO NPs were analyzed using SEM images. Figure 3a, c show the SEM images, and (b) and (d) show the particle size distributions of pure ZnO and 5% AgCu/ZnO NPs, respectively (see Supplementary Information Fig. S2 for Ag, Cu, and bimetallic 10% AgCu-decorated ZnO NPs). The ZnO morphology exhibited a spherical shape with a uniform particle size distribution of approximately 50 nm. Similar size distributions were observed for pure Cu/ZnO, Ag/ZnO, bimetallic 5AgCu/ZnO, and 10AgCu/ZnO NPs,

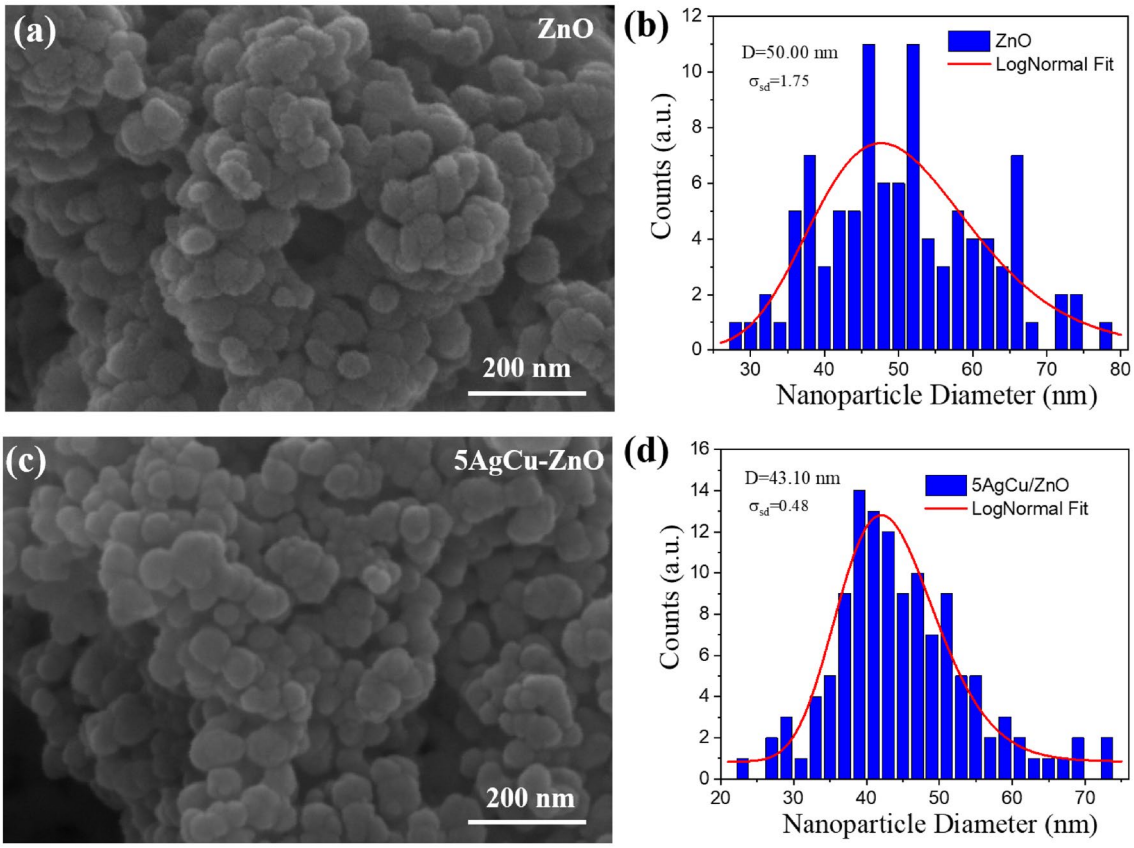


Fig. 3 **a** and **c** SEM images of pure ZnO and 5AgCu/ZnO NPs. **b** and **d** present the particle size distribution of pure ZnO and 5AgCu/ZnO (blue bar) with a lognormal fit (red line) (Color figure online)

measuring approximately 46, 59, 43, and 49 nm (see Table 1). The shape of the NPs was expected based on the synthesis conditions because the NP shape is highly dependent on the alkaline and hydrolysis ratios. The use of minimal water content results in the formation of spherical nanoparticles [42, 43].

Figure 4a–d show the EDS spectra and elemental analysis of ZnO (black), Cu/ZnO (red), Ag/ZnO (green), and bimetallic 5AgCu/ZnO (blue) NPs, respectively. The inset tables show the elemental analysis of Zn, O, Ag, and Cu with atomic percentages. These results provide clear evidence for the reduction of mono Ag, Cu, and bimetallic AgCu on ZnO. The differences in the atomic ratios compared to the aimed initial ratios may be attributed to the different reduction and nucleation rates between Ag and Cu [44, 45]. The peak at around 2.12 keV indicates the presence of Au due to surface coating for improved imaging processes. The EDS results confirm the presence of Ag, Cu, and AgCu nanoparticles, aligning well with the XRD results.

3.4 Optical properties

Figure 5a shows the UV–Vis absorption spectra of ZnO (black), Cu/ZnO (red), Ag/ZnO (green), bimetallic 5AgCu/ZnO (blue), and 10AgCu/ZnO (brown) NPs. Small amounts of NPs were dispersed in an ethanol solution, and UV–Vis measurements were performed to obtain the absorbance spectra. The spectrum exhibited a maximum absorption peak at a wavelength of 373 nm, which is a characteristic peak corresponding to the bandgap absorption of ZnO NPs [46]. There was no pronounced absorbance peak corresponding to Ag or Cu nanoparticles, possibly because of their smaller amount compared to that of ZnO. However, the observed shift in the spectrum from 373 to 376 nm was primarily caused by mono Ag, Cu, and bimetallic AgCu NPs [46]. Previous studies have suggested that Ag–Cu NPs usually form core–shell structures with optical properties similar to those of pure Ag, with a characterized absorption peak around 380 nm [44]. In the case of the separate phases of bimetallic NPs,

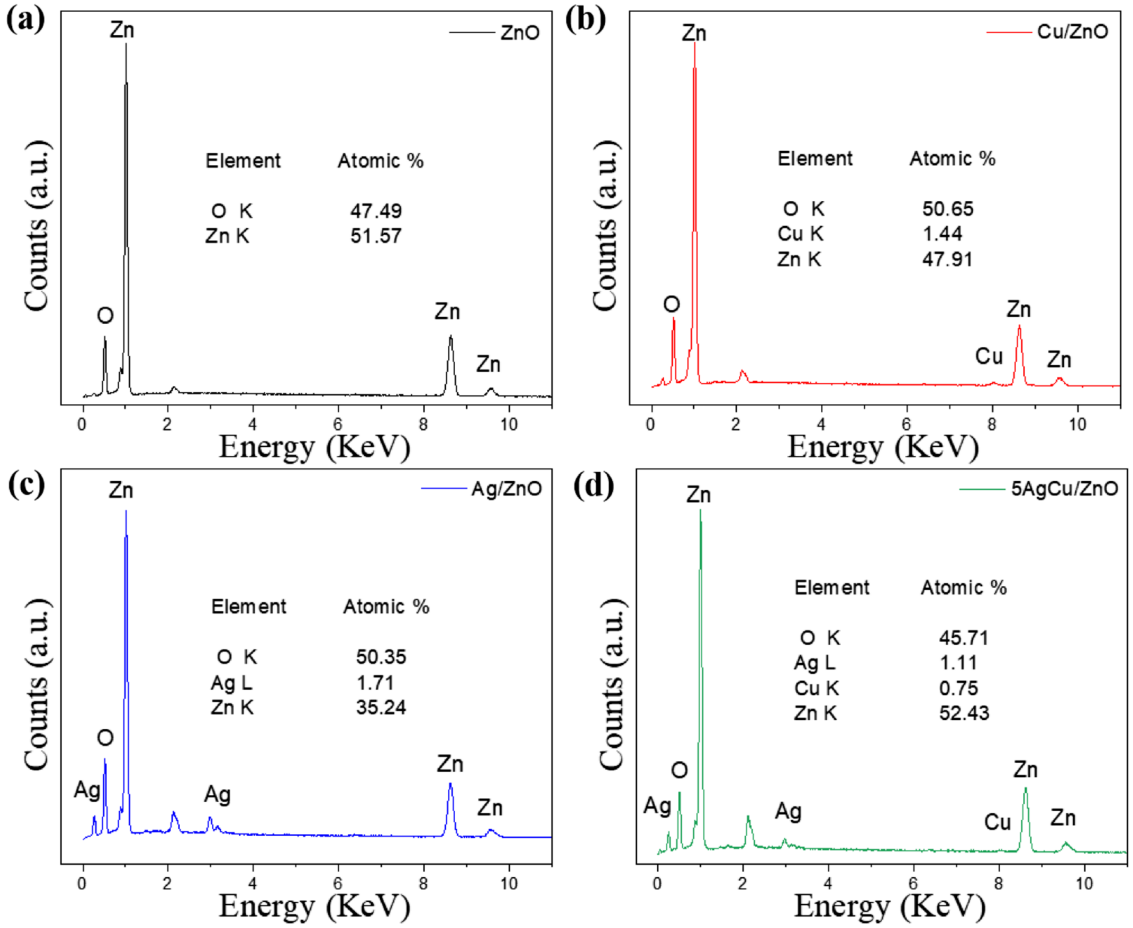


Fig. 4 EDS spectra and elemental analysis of ZnO (black), Cu/ZnO (red), Ag/ZnO (green), and bimetallic 5AgCu/ZnO (blue) NPs (Color figure online)

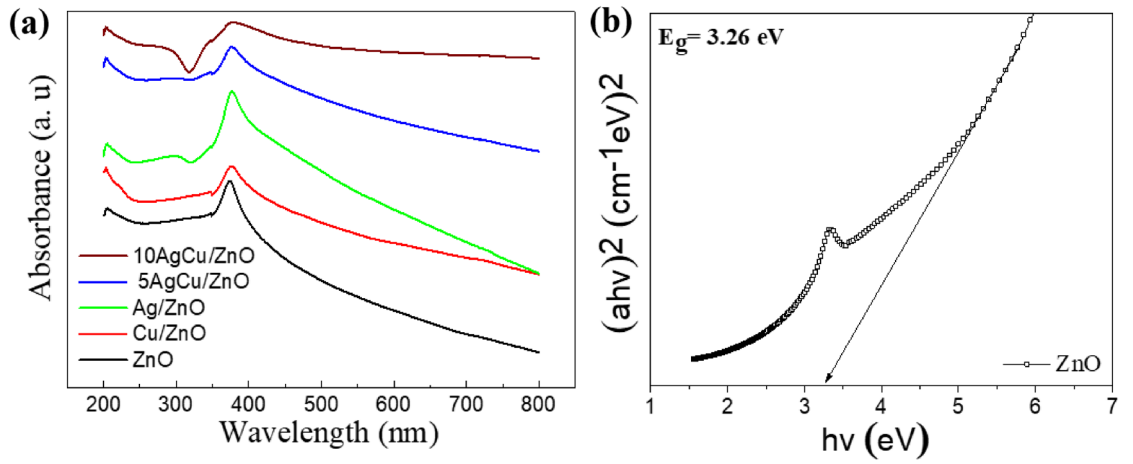


Fig. 5 **a** UV–Vis absorption spectra of ZnO (black), Cu/ZnO (red), Ag/ZnO (green), bimetallic 5AgCu/ZnO (blue), and 10AgCu/ZnO (brown) NPs. **b** $(\alpha h\nu)^2$ versus photon energy (hυ) plot for ZnO NPs showing the band gap value (Color figure online)

the optical absorption peaks belong to each element or show merged peaks between Ag and Cu. Furthermore, the reduction of AgCu commonly results in Ag-rich Cu, even if the initial Ag/Cu ratio is 1, suggesting that copper might not have undergone complete reduction during the synthesis (as evident from the EDS results) [44, 45]. This confirmed that the optical properties of 5AgCu (with separated bimetallic phases) and 10AgCu (with an alloy structure) were more likely to be similar to those of pure Ag.

Based on these results and the shape of the optical absorption peaks, it can be stated that the prepared 10AgCu NPs mostly exhibit a core–shell structure, similar to earlier findings [47, 48]. However, a noteworthy decrease in the absorbance intensity of the ZnO peak indicates the presence of silver and copper on the ZnO surface. The common method to estimate the band gap E_g is to use Tauc's equation. For direct band gap transitions in ZnO, E_g can be calculated using the following formula [49]:

$$(\alpha h\upsilon)^2 = B\left(h\upsilon - E_g\right) \quad (3)$$

where $h\upsilon$ is the energy of the incident photons, B is a constant, and α is the absorption coefficient. The values of E_g were determined by the intersection of the extrapolated linear part of the $(\alpha h\upsilon)^2$ curves with the photon energy ($h\upsilon$) axis, as shown in the inset of Fig. 5b for the case of ZnO NPs (see Supplementary Information Fig. S3 for the other samples). The optical band gap values were found to be 3.26, 3.20, 3.15, 3.35, and 3.37 eV for ZnO, Ag/ZnO, Cu/ZnO, 5AgCu/ZnO, and 10AgCu/ZnO NPs, respectively.

3.5 Photocatalytic activity

The photocatalytic activity of the NPs was evaluated by degrading MB dye in an aqueous solution under both direct sunlight irradiation and UV light for up to 120 min. The results were obtained using UV–Vis spectroscopy in the 400–800 nm range. The maximum absorption peak of MB shifted to shorter wavelengths, which was attributed to the formation of intermediates resulting from the MB degradation mechanism. Other studies have reported similar results [50, 51]. Overall, the photocatalytic activities of pure ZnO, mono Ag/ZnO, Cu/ZnO, and bimetallic (5, 10) AgCu/ZnO NPs were compared, and enhanced activities were observed.

3.5.1 *Photocatalytic degradation of MB dye under UV light*

Under UV light, the photocatalytic performance of the prepared samples was studied by measuring the decrease in the intensity of the maximum absorption peaks at 20-min intervals from 0 to 120 min. Figure 6 illustrates the absorption spectra and degradation rate of MB. It can be observed that ZnO exhibited the lowest degradation rate of 74.28%, followed by Cu/ZnO at 89.50%, 5AgCu/ZnO with 90.06%, Ag/ZnO with 92.06%, and 10AgCu/ZnO with 95.43%. These results clearly indicate the role of plasmonic effects in enhancing photocatalytic activity, with Ag showing a more pronounced effect under UV irradiation than Cu. In the case of AgCu alloy, the combination of plasmon resonances from both Ag and Cu results in synergistic plasmonic effects, which differ from those of pure Ag and Cu. These synergistic plasmonic effects are expected to be lower than those of Ag nanoparticles (red-shifted compared to pure Ag) but higher than those of Cu nanoparticles (blue-shifted compared to pure Cu). The behavior of the bimetallic nanoparticle system can be tuned by controlling the composition ratio, which impacts the plasmonic resonance wavelengths and the efficiency of charge separation resulting from the metal/semiconductor heterojunction. Therefore, it can be concluded that plasmonic effects are a crucial parameter affecting the overall photocatalytic performance by enhancing the absorption of higher energy photons (under UV).

3.5.2 *Photocatalytic degradation of MB dye under sunlight*

The photocatalytic activity of the prepared samples was evaluated through the photodegradation of MB under direct natural sunlight by measuring the decrease in the intensity of the maximum absorption peaks at 20-min intervals. In contrast to the photocatalytic performance under UV light, the bimetallic/ZnO NPs exhibited a drawback under sunlight, as shown in Fig. 7 The lowest degradation rate was recorded for ZnO at 81%, followed by 5AgCu/ZnO at 87.72%, 10AgCu/ZnO at 94.44%, Ag/ZnO at 98.34%, and Cu/ZnO at 98.86%. This difference in efficiency between ZnO under solar and UV light can be attributed to the lower UV source used in this experiment

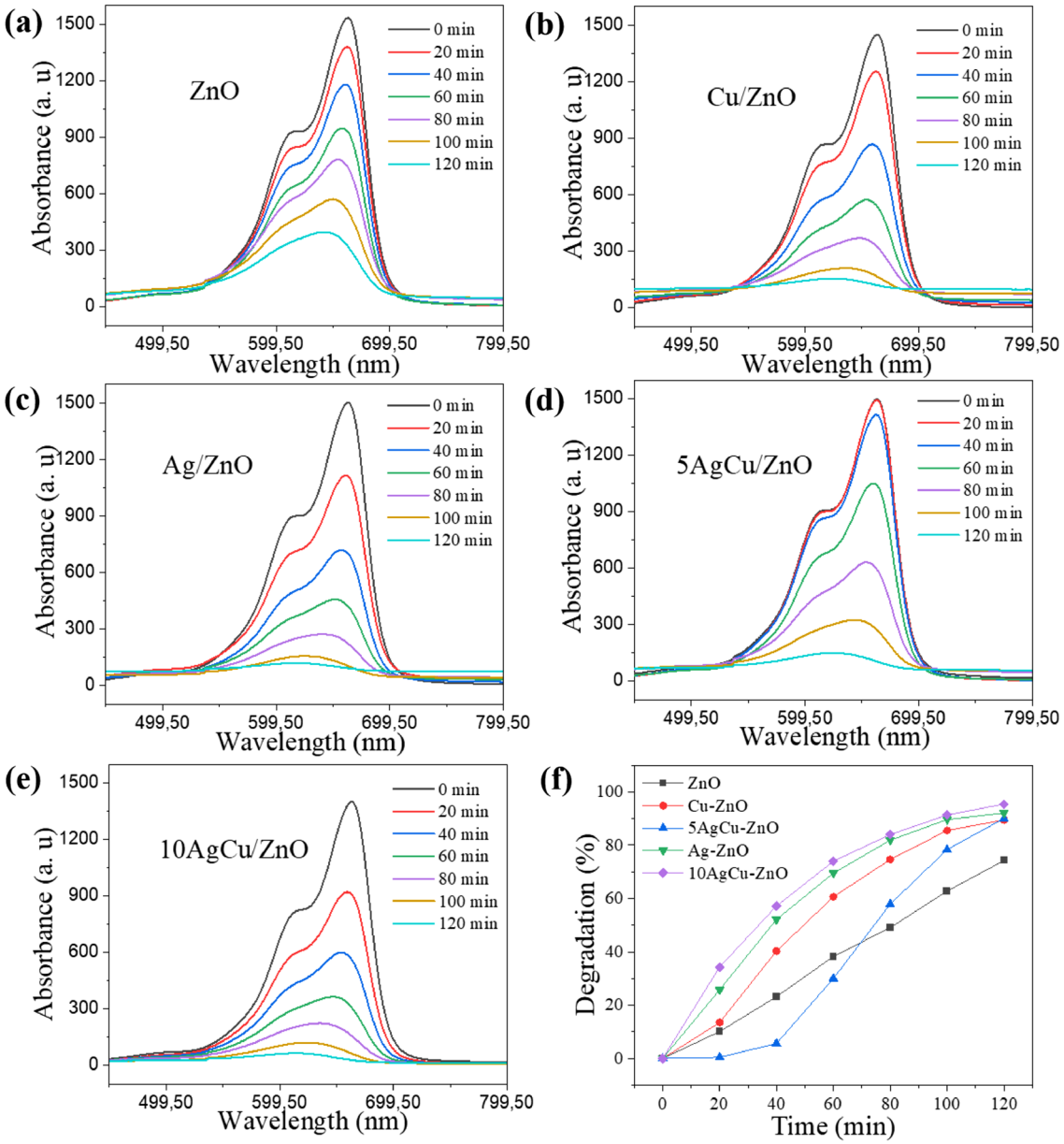


Fig. 6 **a–e** UV–Vis absorption spectra of MB dye in the presence of NPs under UV light ZnO, Cu/ZnO, Ag/ZnO, bimetallic 5AgCu/ZnO, and 10AgCu/ZnO NPs, respectively. **f** Degradation efficiency of MB dye by NPs under UV light as a function of time

(9 W). Monometallic Ag and Cu exhibited better performance, which was expected due to the increased efficiency of bare ZnO and the plasmonic nature of Ag and Cu, leading to enhanced absorption in the visible region. This enhancement is supported by the better efficiency of Cu/ZnO, where Cu nanoparticles have plasmon resonances that extend more into the visible-light region than Ag nanoparticles, which exhibit plasmonic effects mainly in the UV region, as discussed previously. The Ag and Cu monometallic nanoparticles showed surface plasmon resonances (SPR) at 480 and 640 nm, respectively [51]. Surprisingly, however, the bimetallic AgCu/ZnO exhibited significantly lower performance than monometallic/ZnO counterparts under sunlight.

This contradiction with the UV results reported in a similar study for Au–Pt alloyed with TiO_2 can be explained as follows: The better photocatalytic activity of Au–Pt alloyed nanoparticles compared to the single metals under UV is attributed to the higher number of

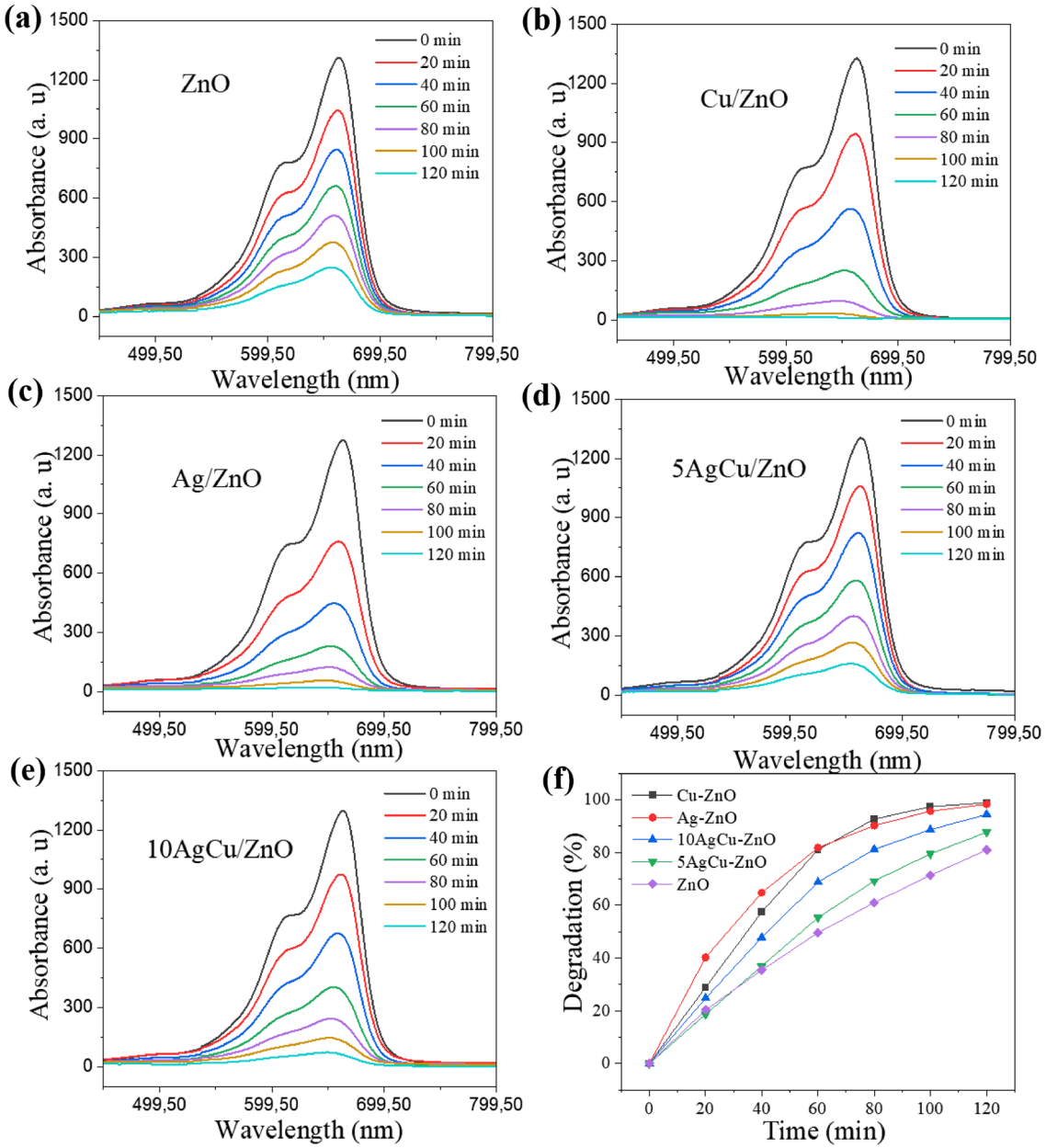


Fig. 7 **a–e** UV–Vis absorption spectra of MB dye in the presence of NPs under sunlight ZnO, Cu/ZnO, Ag/ZnO, bimetallic 5AgCu/ZnO and 10AgCu/ZnO NPs, respectively. **f** The degradation efficiency of MB dye by NPs under sunlight as a function of time

electrons primarily photogenerated by TiO_2. Stronger interactions between the alloyed structures and the TiO_2 support improve the charge separation. However, under visible light, photons can be absorbed by Au NPs, but the presence of nonplasmonic Pt reduces light adsorption and activity [52, 53]. In this work, both Ag and Cu are plasmonic materials, and their absorption should increase (leading to more charge carriers) in the visible-light region. However, the lower activity of bimetallic NPs compared to that of monometallic NPs can be explained by considering another critical factor in photocatalysis: the separation of charge carriers and the prevention of fast recombination. This why Ag, Cu, and bimetallic NPs are used as co-catalysts. The bimetallic system provides evidence of the significance of this role. For instance, 10AgCu/ZnO, which contains 5% Ag and 5% Cu, is expected to absorb more visible light and generate more charges. Nevertheless,

it exhibited lower effectiveness than Cu/ZnO (containing 5% Cu) and Ag/ZnO (containing 5% Ag).

The electron transfer pathways within the interfaces may control the overall outcome. It has been reported that hot electrons are injected from Cu and Ag into TiO2 in monometallic systems. In contrast, in an AgCu bimetallic system, Cu receives hot electrons injected by Ag and then transfers them to TiO_2. During this process, it has been observed that the number of electrons received by Cu from Ag is far less than that gathered at the Ag/TiO_2 interface [41]. Therefore, the movement of charges is more efficient in monometallic systems than in bimetallic systems. Notably, the charge carriers generated under sunlight have less energy than those generated under UV light, implying lower mobility and potentially more recombination, thereby hindering the efficiency. Additionally, the movement paths of photogenerated electrons and the migration path of hot electrons are in opposite directions, causing some hot electrons to flow back into the metal [54].

However, it is essential to mention that the composition ratio remains an influencing factor, further confirming the significance of plasmonic effects. This can be deduced from the results of 5AgCu/ZnO, which exhibited a lower efficiency than 10AgCu/ZnO. In comparison to other binary ratios and single metals, a binary system of Ag and Cu (1Ag–2Cu)/TiO_2 has been reported to extend optical absorption, facilitate efficient charge separation, and exhibit superior photocatalytic activities [51]. Ag_xAu_{1-x} NPs were deposited on ZIS sheets; the importance of the composition ratio of Ag_xAu_{1-x} for generating more charge carriers and facilitating their transfer and separation has been highlighted [55]. The rate constants were calculated using Eq. (2) and are presented in Fig. 8. It is evident from the rate constants and degradation efficiencies obtained that Cu/ZnO NPs are the most effective photocatalysts among all the samples under sunlight, with a constant rate of 0.039 min^{-1} and a degradation efficiency of 98.86%. The obtained results are compared with other studies which used ZnO for the degradation of MB as shown in Table 2.

The mechanism of MB photodegradation primarily begins with the absorption of photons with energies equal to or higher than the photocatalyst band gap as shown in Fig. 9. Consequently, electrons are excited to the conduction band (CB), leaving behind holes in the valence band (VB). The electron–hole pairs then migrate to the photocatalyst surface and react with O_2/OH^- to generate reactive oxygen species ($\cdot O_2^-$) and active hydroxyl radicals (·OH). These species are responsible for the degradation of the organic compounds in the MB dyes, ultimately converting them into CO_2 and H_2O.

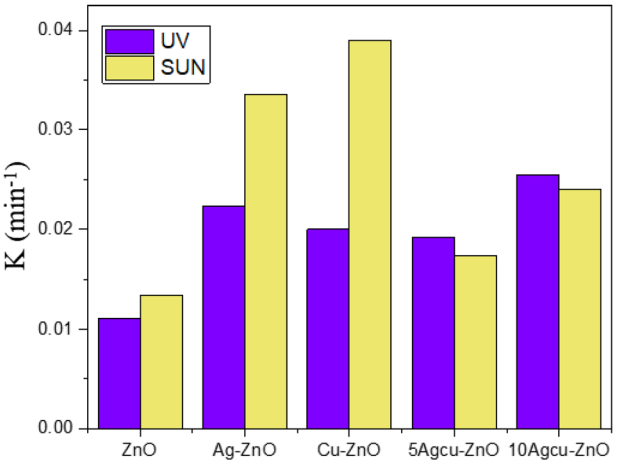


Fig. 8 Constant rate of all NPs for UV and sunlight

Regarding the Ag, Cu, and AgCu/ZnO nanocomposite mechanism under solar light, metallic plasmonic nanoparticles essentially act as dye sensitizers, absorbing resonant photons and transferring the generated electrons to the nearby semiconductor [60]. Whereas under UV light the electrons transfer from ZnO to Ag, Cu, and AgCu nanoparticles surface and enhance the separation of photogenerated electron–hole pairs. The difference between the Fermi level of ZnO (5.4 eV) and the work function of Ag, Cu, and AgCu alloy NPs leads to the formation of an ohmic junction upon contact with the metal/semiconductor system. The work function values are as follows: Ag (4.3 eV), Cu (4.6 eV), and the work function of the AgCu NPs is proposed to be in the range between 4.3 eV and 4.6 eV [61, 62]. This difference in work function facilitates effective charge separation and reduces unfavorable recombination, with electrons transferring between Ag, Cu, and AgCu NPs and ZnO, thus enhancing the photocatalytic activity [63]. Furthermore, Sarika Singh reported that even in the monometallic system Ag (1, 3. And 5wt%) decorated ZnO the transfer of electrons under UV and sunlight irradiation is different [58]. Herein this work, it was found that the transfer of electrons in the monometallic/ZnO and bimetallic/ZnO systems are different and the simpler monometallic/ZnO system exhibited better and more effective charge

Table 2 Comparison of the MB degradation efficiency of the present work with literature

Photocatalysts	Catalyst concentrations (g/L)	MB concentration (ppm)	Photon source	Efficiency (%)	Irradiation time (min)	Reference
ZnO	0.1	10	a visible lamp with 250-w, 400–700 nm	90	120	[56]
6% Cu-doped ZnO	1	20	sunlight	89	180	[57]
3wt% Ag decorted ZnO	0.3	10	UVA 365 nm 25W + UVC 254 nm 30W	99	40	[58]
1wt% Ag decorted ZnO	0.3	10	sunlight	100	180	
1% Ag doped ZnO	0.6	10	sunlight	98	120	[59]
10% AgCu/ZnO	0.2	10	UV lamp 254 nm 9W	95	120	Present work
5% Cu/ZnO	0.2	10	sunlight	99	120	
5% Ag/ZnO	–	–	–	98	–	

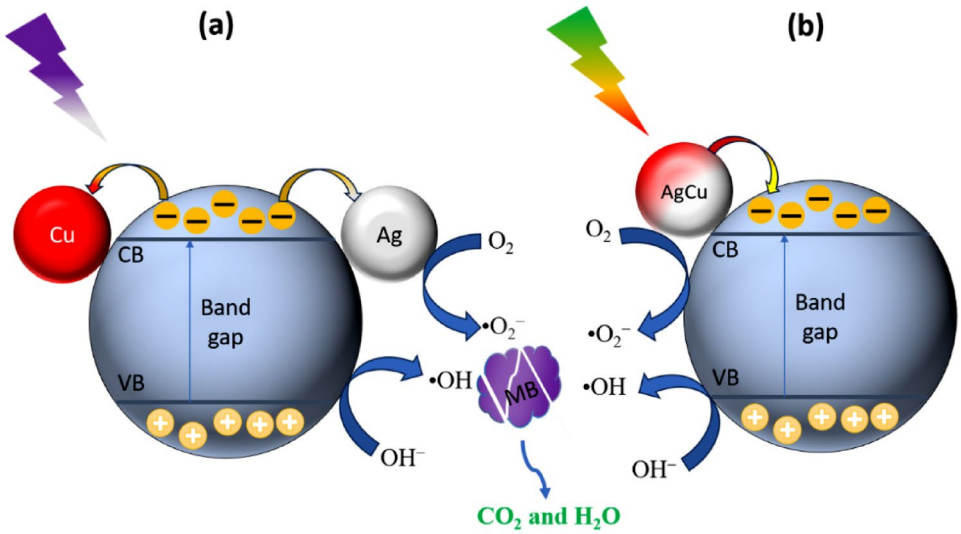


Fig. 9 Photocatalytic mechanism of monometallic (Ag, Cu)/ZnO system and bimetallic AgCu/ZnO system nanocomposite for photocatalytic degradation of MB in the presence of **a** UV light and **b** solar light irradiation

separation performance under sunlight than the bimetallic/ZnO system.

4 Conclusion

In this study, monometallic Ag, Cu, and bimetallic AgCu nanoparticles were successfully synthesized using a modified polyol process and deposited onto ZnO nanoparticles. The structural characterization through X-ray diffraction (XRD) analysis, supported by Rietveld refinement, confirmed the presence of the hexagonal wurtzite structure of ZnO and cubic phases of both Ag and Cu in the monometallic and bimetallic AgCu nanoparticles. SEM analysis revealed the spherical morphology of the nanoparticles, with an average particle size of 50 nm. EDS elemental analysis provided evidence of the successful deposition of Ag, Cu, and AgCu nanoparticles onto the ZnO surface. Photocatalytic evaluations were conducted to assess the degradation of methylene blue dye under both UV and sunlight illumination, aiming to investigate the photocatalytic behavior of monometallic and bimetallic systems under different light sources. The results showed that under UV light, the bimetallic/ZnO system demonstrated superior performance, achieving a degradation rate of 95% for 10AgCu/ZnO. However, under sunlight illumination, the bimetallic/ZnO system exhibited a drawback, where as the monometallic/ZnO nanoparticles, particularly Cu/ZnO nanoparticles, displayed exceptional photocatalytic efficiency, with a degradation rate of 99%. The observed inconsistent trends in performance were attributed to the multifaceted

interplay between plasmonic properties and charge transfer mechanisms influencing the photocatalytic activity. Despite the enhancement of absorption in the visible region due to the plasmonic properties of Ag and Cu, the charge transfer mechanism within the monometallic/ZnO system facilitated facile electron injection, leading to superior photocatalytic efficiency compared to the bimetallic/ZnO system. This study highlights the role of plasmonic metals and their interactions with the support semiconductors for efficient charge-transfer mechanisms in photocatalysis.

Acknowledgements

This study was conducted at the Advanced Materials and Nanotechnology Research Group laboratory, Cukurova University. A Noua is a postdoctoral research fellow supported by the Research Scholarship Program of Turkiye Scholarships.

Author contributions

Abd Elouahab Noua: Data curation, Formal analysis, Validation, Roles/Writing—original draft, Writing—review & editing, Investigation, Methodology. Dogan Kaya: Conceptualization, Formal analysis, Funding acquisition, Investigation, Methodology, Project administration, Validation, Roles/Writing—original draft, Writing—review and editing. Gokmen Sigircik: Conceptualization, Methodology, Roles/Writing—review & editing. Tunc Tuken: Conceptualization, Methodology, Roles/Writing—review and editing. Faruk Karadag: Conceptualization, Funding acquisition, Methodology, Project administration, Roles/Writing—review & editing. Ahmet Ekicibil: Conceptualization, Funding acquisition, Methodology, Project administration, Roles/Writing—review & editing.

Funding

Open access funding provided by the Scientific and Technological Research Council of Türkiye (TÜBİTAK). The authors have not disclosed any funding.

Data availability

All data generated or analyzed during this study are included in this published article (and its supplementary information files).

Declarations

Conflict of interest The authors declare that they have no known competing financial interests or personal relationships that could have influenced the work reported in this study.

Supplementary Information The online version contains supplementary material available at https://doi.org/10.1007/s10854-024-12919-4.

Open Access This article is licensed under a Creative Commons Attribution 4.0 International License, which permits use, sharing, adaptation, distribution and reproduction in any medium or format, as long as you give appropriate credit to the original author(s) and the source, provide a link to the Creative Commons licence, and indicate if changes were made. The images or other third party material in this article are included in the article's Creative Commons licence, unless indicated otherwise in a credit line to the material. If material is not included in the article's Creative Commons licence and your intended use is not permitted by statutory regulation or exceeds the permitted use, you will need to obtain permission directly from the copyright holder. To view a copy of this licence, visit http://creativecommons.org/licenses/by/4.0/.

References

1. R. Gusain, K. Gupta, P. Joshi et al., Adv. Colloid Interface Sci. **272**, 102009 (2019)
2. A. Modwi, M.A. Abbo, E.A. Hassan et al., J. Mater. Sci. Mater. Electron. **27**, 12974–12984 (2016)
3. A. Fujishima, K. Honda, Nature **238**, 37–38 (1972)

4. H. Karimi-Maleh, B.G. Kumar, S. Rajendran et al., J. Mol. Liq. **314**, 113588 (2020)
5. S. Ali, J. Abdul Nasir, R. Nasir Dara et al., Inorg. Chem. Commun. **145**, 110011 (2022)
6. M. Iqbal, A. Ibrar, A. Ali et al., J. Mol. Struct. **1267**, 133598 (2022)
7. K. Qi, B. Cheng, J. Yu et al., J. Alloys Compd. **727**, 792–820 (2017)
8. R.H. Waghchaure, V.A. Adole, B.S. Jagdale, Inorg. Chem. Commun. **143**, 109764 (2022)
9. G.K. Weldegebrieal, Inorg. Chem. Commun. **120**, 108140 (2020)
10. T. Saidani, M. Zaabat, M.S. Aida et al., Superlattices Microstruct. **88**, 315–322 (2015)
11. T.M. Bawazeer, M.S. Alsoufi, M. Shkir et al., Inorg. Chem. Commun. **130**, 108668 (2021)
12. N.R. Khalid, A. Hammad, M.B. Tahir et al., Ceram. Int. **45**, 21430–21435 (2019)
13. F.M. Sanakousar, C.C. Vidyasagar, V.M. Jiménez-Pérez et al., Mater. Sci. Semicond. Process. **140**, 106390 (2022)
14. N. Elamin, A. Modwi, M.B. Aissa, K.K. Taha, O.K. Al-Duaij, T.A. Yousef, J. Mater. Sci. Mater. Electron. **32**, 2234–2248 (2021)
15. K. Mubeen, A. Irshad, A. Safeen et al., J. Saudi Chem. Soc. **27**, 101639 (2023)
16. E. Abel Noelson, M. Anandkumar, M. Marikkannan et al., Chem. Phys. Lett. **796**, 139566 (2022)
17. R. Kavitha, S.G. Kumar, Mater. Sci. Semicond. Process. **93**, 59–91 (2019)
18. H. Sun, S.-Y. Lee, S.-J. Park, J. Colloid Interface Sci. **629**, 87–96 (2023)
19. P. Cheng, Y. Wang, L. Xu et al., Mater. Lett. **175**, 52–55 (2016)
20. D.L. Liao, B.Q. Liao, J. Photochem. Photobiol. A: Chem. **187**, 363–369 (2007)
21. N. Talebian, M.R. Nilforoushan, N. Maleki, Thin Solid Films **527**, 50–58 (2013)
22. R. Saravanan, E. Thirumal, V.K. Gupta et al., J. Mol. Liq. **177**, 394–401 (2013)
23. M. Lal, P. Sharma, C. Ram, Results Optics. **10**, 100371 (2023)
24. H.R. Khan, G. Murtaza, M.A. Choudhary et al., Sol. Energy **173**, 875–881 (2018)
25. M. Ahmad, W. Rehman, M.M. Khan et al., J. Environ. Chem. Eng. **9**, 104725 (2021)
26. Y. Liu, Q. Zhang, M. Xu et al., Appl. Surf. Sci. **476**, 632–640 (2019)
27. V. Vaiano, C.A. Jaramillo-Paez, M. Matarangolo et al., Mater. Res. Bull. **112**, 251–260 (2019)
28. S. Li, P. Miao, Y. Zhang et al., Adv. Mater. **33**, 2000086 (2021)
29. K.V. Karthik, A.V. Raghu, K.R. Reddy et al., Chemosphere **287**, 132081 (2022)
30. M.K. Aulakh, S. Kaur, B. Pal et al., Solid State Sci. **99**, 106045 (2020)
31. S. Vivek, S. Preethi, K.S. Babu, Mater. Chem. Phys. **278**, 125669 (2022)
32. D. Kaya, J. Mater. Sci. Mater. Electron. **32**, 27975–27986 (2021)
33. M.T. Islam, H. Jing, T. Yang et al., J. Environ. Chem. Eng. **6**, 3827–3836 (2018). https://doi.org/10.1016/j.jece.2018.05.032
34. A. Meng, J. Xing, Z. Li et al., ACS Appl. Mater. Int **7**, 27449–27457 (2015)
35. M.F. Khan, A.H. Ansari, M. Hameedullah et al., Sci. Rep. 6, 27689 (2016)
36. R. Kumari, A. Sahai, N. Goswami, Prog. Natural Sci.: Mater. Int. **25**, 300–309 (2015)
37. Q. Dou, Y. Li, K.W. Wong et al., J. Mater. Res. **34**, 2095–2104 (2019)
38. H.R. Tantawy, A.A. Nada, A. Baraka et al., Appl. Surf. Sci. Adv. **3**, 100056 (2021)
39. A. Abdul Salam, R. Singaravelan, P. Vasanthi et al., J. Nanostructure Chem. **5**, 383–392 (2015). https://doi.org/10.1007/s40097-015-0170-1
40. J.R. Deka, D. Saikia, T.-H. Cheng et al., J. Environ. Chem. Eng. **11**, 109777 (2023)
41. L. Sang, Z. Yu, C. Wang et al., Int. J. Hydrog. Energy **48**, 12215–12226 (2023)
42. J. Yin, F. Gao, C. Wei et al., Sci. Rep. **4**, 3736 (2014). https://doi.org/10.1038/srep03736
43. A. Dakhlaoui, M. Jendoubi, L.S. Smiri et al., J. Cryst. Growth. **311**, 3989–3996 (2009). https://doi.org/10.1016/j.jcrysgro.2009.06.028
44. Z. Xiong, F. Qin, P.-S. Huang et al., JOM. **68**, 1163–1168 (2016). https://doi.org/10.1007/s11837-015-1757-1
45. M.B. Cortie, A.M. Mcdonagh, Chem. Rev. **111**, 3713–3735 (2011)
46. P. Fageria, S. Gangopadhyay, S. Pande, RSC Adv. **4**, 24962–24972 (2014)
47. D. Manikandan, S. Mohan, K.G.M. Nair, B. Physica, Condensed Matter. **337**, 64–68 (2003)
48. A. Sakthisabarimoorthi, M. Jose, S. Martin Britto Dhas et al., J. Mater. Sci. Mater. Electron. **28**, 4545–4552 (2017). https://doi.org/10.1007/s10854-016-6090-0
49. J. Tauc, Mater. Res. Bull. **3**, 37–46 (1968)
50. S. De Quadros, Horst Pereira Metz DC, Zimmermann LM. J. Phys. Chem. Solids **181**, 111464 (2023)

51. S. Bhardwaj, B. Pal, Adv. Powder Technol. **29**, 2119–2128 (2018)
52. F. Wang, Y. Jiang, D.J. Lawes et al., ACS Catal. **5**, 3924–3931 (2015)
53. Y. Liu, Z. Sun, Y.H. Hu, Chem. Eng. J. **409**, 128250 (2021)
54. X. Zhang, Y. Zhu, X. Yang et al., Nanoscale **5**, 3359–3366 (2013). https://doi.org/10.1039/C3NR00044C
55. H. An, M. Li, R. Liu et al., Chem. Eng. J. **382**, 122953 (2020)
56. A. Bhapkar, R. Prasad, D. Jaspal et al., Inorg. Chem. Commun. **148**, 110311 (2023)
57. S. Sivakumar, Y. Robinson, N.A. Mala, Appl. Surf. Sci. Adv. **12**, 100344 (2022)
58. S. Singh, Mater. Today Commun.. **33**, 104438 (2022)
59. M.A. Kareem, I.T. Bello, H.A. Shittu et al., Clean. Mater. **3**, 100041 (2022)
60. S. Linic, P. Christopher, Ingram DBJNM **10**, 911–921 (2011)
61. B. Sarma, B.K. Sarma, Appl. Surf. Sci. **410**, 557–565 (2017)
62. P.O. Gartland, S. Berge, B.J. Slagsvold, Phys. Rev. Lett. **28**, 738–739 (1972)
63. V. Fauzia, A. Yudiana, Y. Yulizar et al., J. Phys. Chem. Solids **154**, 110038 (2021)

Publisher's Note Springer Nature remains neutral with regard to jurisdictional claims in published maps and institutional affiliations.